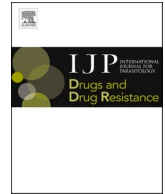






Contents lists available at ScienceDirect

International Journal for Parasitology: Drugs and Drug Resistance

journal homepage: www.elsevier.com/locate/ijpddr

Nitroxoline evidence amoebicidal activity against *Acanthamoeba castellanii* through DNA damage and the stress response pathways

Lijun Chen^a, Wei Han^b , Wenwen Jing^a, Meng Feng^a, Qingtong Zhou^{c,*}, Xunjia Cheng^{a,*} ^a Department of Medical Microbiology and Parasitology, School of Basic Medical Sciences, Fudan University, Shanghai, China^b Translational Center for Medical Structural Biology, Ruijin Hospital, Shanghai Jiao Tong University School of Medicine, Shanghai, China^c Department of Pharmacology, School of Basic Medical Sciences, Fudan University, Shanghai, China

ARTICLE INFO

Keywords:

Nitroxoline

Acanthamoeba castellanii

Transcriptomics

Molecular docking

ABSTRACT

Acanthamoeba castellanii is a widespread unicellular eukaryote found in diverse environments, including tap water, soil, and swimming pools. It is responsible for severe infections, such as *Acanthamoeba* keratitis and granulomatous amoebic encephalitis, particularly in individuals with immunocompromise. The ability of protozoans to form dormant and persistent cysts complicates treatment, as current therapies are ineffective against cyst stages and suffer from poor specificity and side effects. Nitroxoline, a quinoline derivative with well-established antibacterial, antifungal, and antiviral properties, is a promising therapeutic candidate. This study aimed to elucidate cellular signalling events that counteract the effects of nitroxoline. In this study, nitroxoline significantly reduced the viability of *A. castellanii* trophozoites in a dose- and time-dependent manner, inducing morphological changes and apoptosis. Transcriptomic analysis revealed substantial alterations in gene expression, including enrichment of metabolic pathways, DNA damage responses, and iron ion binding. Nitroxoline treatment upregulated genes involved in DNA repair and oxidative stress response while regulating genes in the methionine and cysteine cycles. It also decreased the mitochondrial membrane potential, H₂S production, and total iron amount in *A. castellanii*. Bioinformatic analyses and molecular docking studies suggest direct interactions between nitroxoline and several *A. castellanii* proteins. Our research provides a comprehensive molecular map of the response of *A. castellanii* to nitroxoline, revealing significant changes in gene expression related to the stress response and metabolic pathways. These findings underscore the potential of nitroxoline as a potent anti-*Acanthamoeba* agent, offering new insights into its mechanism of action and paving the way for effective combinational therapeutic strategies.

1. Introduction

Acanthamoeba castellanii is a cosmopolitan unicellular eukaryotic organism commonly found in tap water, swimming pools, soil, cooling towers, and drinking water networks. Free-living Amoeba including *Acanthamoeba* species, are opportunistic protist with a widespread distribution worldwide (Visvesvara et al., 2007; Siddiqui and Khan, 2012; Zhang and Cheng, 2021). In humans, various *Acanthamoeba* species can cause a sight-threatening disease named, *Acanthamoeba* keratitis (AK), which is the more common disease seen by *Acanthamoeba*, found more commonly in contact lens misuse by wearers (Cabrera-Aguas et al., 2022; Niederkorn, 2021). In immunocompromised patients, *Acanthamoeba* can cause chronic infectious ulcers, cutaneous lesions, and

furthermore, through systemic dissemination, make its way to the brain causing a normally fatal disease granulomatous amoebic encephalitis (GAE) (Kalra et al., 2020; Wang et al., 2021; Damhorst et al., 2022). *Acanthamoeba* can cause AK in immunocompetent individuals, and its distribution is limited to the eye, where it can cause keratitis and blindness, if not diagnosed early, treated appropriately and aggressively. A study estimated that the global incidence of AK is 2.9 cases per million people with an increasing trend in incidence observed in some regions (Y. Zhang et al., 2023).

Acanthamoeba also has the innate ability to survive under harsh environmental conditions and sub-lethal drug exposure without genetic resistance by transiently stopping their growth, slowing their metabolism, and eventually shifting to dormant and persistent cysts. A

* Corresponding author.

** Corresponding author.

E-mail addresses: zhouqt@fudan.edu.cn (Q. Zhou), xjcheng@shmu.edu.cn (X. Cheng).<https://doi.org/10.1016/j.ijpddr.2025.100578>

Received 8 November 2024; Received in revised form 25 December 2024; Accepted 1 January 2025

Available online 4 January 2025

2211-3207/© 2025 The Authors. Published by Elsevier Ltd on behalf of Australian Society for Parasitology. This is an open access article under the CC BY-NC-ND license (<http://creativecommons.org/licenses/by-nc-nd/4.0/>).

conceptually compelling but sparsely investigated approach for identifying useful potentiators involves disrupting the general defence systems that protect pathogens from diverse antibiotics. Currently, no effective anti-*Acanthamoeba* therapies are available. Therefore, innovative anti-*Acanthamoeba* drugs are urgently required. Most current anti-*Acanthamoeba* drugs target the trophozoite-stage parasites. Although cyst-stage parasites do not cause clinical symptoms, drugs that inhibit these two stages are essential for preventing epidemics and protecting vulnerable populations, owing to the increase in anti-*Acanthamoeba* clinical treatment resistance (Elder et al., 1994; Lim et al., 2008; Huang et al., 2021). Chemotherapy for *Acanthamoeba* infections remains challenging due to incomplete knowledge of its complicated pathophysiology. In cases of infection, the treatment regimen is often ineffective owing to delayed diagnosis, poor specificity, and side effects. However, this route is lengthy, with many hurdles and failures, including target specificity, poor pharmacodynamics, pharmacokinetics, and toxicity.

Considering the limited number of anti-*Acanthamoeba* agents, screening of potential anti-*Acanthamoeba* agents from natural products or approved drugs is warranted. Nitroloxline, a quinoline derivative (8-hydroxy-5-nitroquinoline), is a historically used oral antibacterial drug (O'Grady and Smith, 1966) that is structurally distinct from other antibiotics. In addition to its antitumor effects, it is active against numerous human pathogens, including multidrug-resistant bacteria, fungi, and viruses (Fuchs et al., 2021, 2022a, 2022b; Joaquim et al., 2021). Its antibacterial properties are based on the chelation of divalent cations, influencing cell membranes, and inhibiting intracellular enzymes such as RNA polymerase (Hoffmann et al., 2023). From a mechanistic standpoint, nitroloxline partially interferes with the phosphatidylinositol 3-kinase/AKT/mammalian target of rapamycin and rapidly accelerated fibrosarcoma/mitogen-activated protein kinase/extracellular signal-regulated kinase host cell signalling pathways (Bojkova et al., 2023).

Recent studies have also indicated that nitroloxline is a promising drug against free-living pathogenic amoebas, including *Naegleria fowleri*, *Balamuthia mandrillaris*, and *Acanthamoeba* species (Haston and Cope, 2023; Laurie et al., 2018; Rodríguez-Expósito et al., 2023). Although transcriptomic and proteomic analyses have been performed on these free-living amoebae, the signalling pathways involved in their stress responses remain limited. Furthermore, our knowledge of the transcriptomic landscape during nitroloxline treatment remains limited. This study aimed to elucidate the cellular signalling events that counteract the effects of nitroloxline.

2. Materials and methods

2.1. Amoeba cultivation and cysticidal activity assay

Acanthamoeba castellanii (American Type Culture Collection (ATCC) 30011) was obtained from the ATCC. Following established protocols, trophozoites were axenically cultured in a peptone–yeast–glucose medium. This medium comprised 10 g of protease peptone, 10 g of yeast extract, 10 g of glucose, 5 g of NaCl, 0.95 g of L-cysteine, 3.58 g of Na₂HPO₄·12H₂O, and 0.68 g of KH₂PO₄ per litre of deionised distilled water. The culture was incubated at 26 °C, and trophozoites, harvested during the late log phase after 48 h of subculture, were used for subsequent analyses. Encystment was induced through the following procedure: 5 × 10⁶ trophozoites were washed twice with an encystment medium containing 95 mM NaCl, 5 mM KCl, 8 mM MgSO₄, 0.4 mM CaCl₂, 1 mM NaHCO₃, 20 mM Tris-HCl, pH 9.0 and incubated in 10 mL of the encystment medium in the 75 cm² culture flask at 26 °C (Hirukawa et al., 1998). After the encystment process was completed, the cysts were collected and centrifuged at 1000 g for 30 min. Subsequently, 0.5% SDS was used to treat the cysts for 10 min to remove immature cysts. Then, mature cysts were washed three times with PBS and centrifuged at 1000 g for 15 min. Cysts (5 × 10⁵ cysts/mL) were seeded in a 12-well plate and respectively incubated with PYG medium

containing 0.1% DMSO, 20 μM nitroloxline or 40 μM nitroloxline for 72 h. After 3 days of treatment, the medium was replaced with fresh PYG medium, and the culture was continued for recover observation for another 9 days.

2.2. Cell viability assay and IC₅₀ determination

Obtained from TargetMol (Wellesley Hills, MA, USA), nitroloxline was dissolved in 100% dimethyl sulfoxide (DMSO; Sigma-Aldrich, St. Louis, MO, USA) and prepared at 100 mM concentrations. *A. castellanii* trophozoites were seeded at the log growth phase (1 × 10⁴ cells per well) in a 96-well white microplate (Eppendorf, Hamburg, Germany) and incubated with 100 μL of medium containing varied nitroloxline concentrations (2, 4, 6, 8, 10, 12, 14, 16, 18, 20, 40, 60, 80, and 100 μM). And the plates were incubated at 26 °C for 24 h, 48 h, and 72 h and observed under an inverted microscope (Olympus). Cell viability assay results, derived from ≥3 wells per condition and compared with 0.1% DMSO, were evaluated using CellTiter-Glo (Promega, Madison, WI, USA) following the manufacturer's guidelines. Subsequently, 100 μL of CellTiter-Glo reagent was introduced per well, mixed for 2 min on an orbital shaker, and incubated at room temperature for 10 min. Luminescence was recorded on a modular multimode microplate reader (BioTek Synergy H1), and the IC₅₀ values of the compound and growth curves were generated using GraphPad Prism 8. Each experiment was conducted thrice.

2.3. Flow cytometric analysis

Trophozoite apoptosis and reactive oxygen species (ROS) were assessed using a PE Annexin V apoptosis detection kit I (BD Biosciences, San Jose, CA, USA) and a ROS assay kit (Dojindo Molecular Technologies, Inc., Kumamoto, Japan), respectively, following the manufacturer's instructions. *A. castellanii* trophozoites (2 × 10⁶ cells/flask) were cultured with 20 μM and 40 μM nitroloxline for 24 h in 12.5 cm² cell culture flasks (Biofil). Trophozoites were then detached from the flasks, collected in transparent centrifuge tubes (15 mL), and centrifuged at 800 × g for 5 min. These trophozoites (1 × 10⁶ cells/tube) underwent two cold Hanks' balanced salt solution (HBSS) washes and were respectively resuspended in 100 μL of 1 × binding buffer containing 5 μL of PE-Annexin V and 500 μL of ROS working solution containing 0.5 μL of highly sensitive DCFH-DA dye. Subsequently, the trophozoites for apoptosis detection were incubated for 15 min in darkness at room temperature, and 400 μL of 1 × binding buffer was added after incubating. The trophozoites for ROS detection were incubated for 30 min in darkness at room temperature, washed twice with HBSS, and resuspended with 500 μL of HBSS. Fluorescence-activated trophozoite sorting was performed using a FACSAria instrument (BD Biosciences, San Jose, CA, USA) with a 488-nm argon excitation laser. Analysis gates were defined using untreated amoebae, and FlowJo 10.8.1 software (FlowJo LLC, Ashland, OR, USA) was used for data analysis.

2.4. RNA-sequencing (RNA-seq)

Total RNA was isolated from each sample using an RNA mini kit (Qiagen, Hilden, Germany). RNA quality was examined using gel electrophoresis and Qubit (Thermo, Waltham, MA, USA). For RNA sequencing, the RNA samples from three biological replicates at 24 h were separated into three independent pools, each containing two or three distinct samples in equal amounts. The raw data were subsequently analysed as previously described (Chen et al., 2024).

2.5. Real-time quantitative polymerase chain reaction (RT-qPCR)

Total RNA was isolated using the RNeasy Plus Mini Kit (74134; QIAGEN, Hilden, Germany), and cDNA was synthesised using the PrimeScript™ II 1st Strand cDNA Synthesis Kit (6210A; Takara Bio, China).

The reactions (20 μ L per well) were performed in a 96-well plate using 2 μ L of SYBR Premix Ex Taq (Takara, Dalian, Liaoning, China) with 10 μ M primers targeting *A. castellanii* *GNMT*, *CBS*, *GSR*, *PARP*, *MRE11*, *RAD50*, *RAD51*, *DNA2*, *FEN1*, *APE1*, and *DMT1*. Primers for these genes, sourced from published sequences (Table S1), were used for RT-qPCR on an ABI 7500 RT-PCR system (Applied Biosystems, Foster City, CA, USA). The $2^{-\Delta\Delta C_t}$ method was used to calculate the relative expression of each primer between the control and treatment groups, with values normalised to the *18S* reference housekeeping gene (Deng et al., 2015).

2.6. DNA damage determination

Genomic DNA was extracted using the DNeasy Blood & Tissue Kit (Catalogue No. 69506; QIAGEN), following the manufacturer's protocol. DNA concentrations were quantified using a BioPhotometer® D30 (Eppendorf). Trophozoite DNA damage was assessed using the DNA Damage Quantification Kit AP Site Counting (Dojindo, catalogue DK02). DNA was dissolved in TE buffer (10 mM Tris [pH 7.5] and 1 mM EDTA) at 100 μ g/mL, and 10 μ L of purified genomic DNA was mixed with 10 μ L of aldehyde reactive probe (ARP) solution in a MaxyClear microcentrifuge tube (1.5 mL; Corning, NY, USA) and incubated for 1 h at 37 °C. Each ARP-labelled DNA was purified with a filtration tube, and DNA concentration was measured using the BioPhotometer® D30. Purified ARP-derived DNA samples were diluted to 2.25 μ g/mL in TE buffer, and 90 μ L of the ARP-labelled DNA solution was diluted with 310 μ L of TE buffer. Thereafter, 60 μ L of the diluted solution and 100 μ L of DNA binding solution were added to the provided DNA high-binding plate well, incubated overnight at room temperature, and microwells were washed five times in 250 μ L of 1 \times wash buffer. Subsequently, 150 μ L of diluted horseradish peroxidase-streptavidin-enzyme conjugate (1:4000 dilution in 1 \times wash buffer) was added to each well, incubated for 1 h at 37 °C, and microwells were washed five times in 250 μ L of 1 \times wash buffer. After adding 100 μ L of substrate solution, microwells were incubated at 37 °C for 1 h. Absorbance at an optical density (OD) of 650 nm was immediately measured using a modular multimode microplate reader (BioTek Synergy H1).

2.7. Mitochondrial membrane potential (MMP) assay

MMP was evaluated using the MT-1 MitoMP detection kit (MT13, Dojin Kagaku) following the manufacturer's protocol. Treated trophozoites (1 \times 10⁶) were incubated with MT-1 working solution (v:v, 1:1000) for 30 min at 26 °C. After treatment with the MT-1 working solution, the trophozoites were washed twice with HBSS and incubated in an imaging buffer (Kit-provided). Live trophozoite suspensions were placed on glass slides using a Cytospin 4 cytocentrifuge (Thermo Fisher Scientific) and mounted on coverslips. The fluorescence images were obtained using a Leica TCS SP8 microscope, and the fluorescence (λ Ex = 488 nm and λ Em = 580 nm) was measured using a modular multimode microplate reader (BioTek Synergy H1). Images were quantified using ImageJ software (National Institutes of Health, Bethesda, MD, USA).

2.8. Measurement of H₂S production in trophozoites

Following a 24-h treatment, trophozoites (1 \times 10⁶) were washed twice with 1 \times phosphate-buffered saline (PBS) and incubated for 1 h at 26 °C in 500 μ L of HBSS containing 100 μ M of 7-azido-4-methylcoumarin (AzMC) fluorescent probe (802409, Sigma), which selectively reacts with H₂S to form a fluorescent compound. Fluorescent AzMC signal acquisition (λ Ex = 365 nm and λ Em = 450 nm) was performed on a modular multimode microplate reader (BioTek Synergy H1), and the fluorescence images were obtained using a Leica TCS SP8 microscope.

2.9. Intracellular iron assay

The amount of iron (Fe²⁺ and Fe³⁺) was monitored using an iron

assay kit (Dojindo Laboratories Co., Ltd., Kumamoto, Japan). Following a 24-h treatment, trophozoites (2 \times 10⁷) were washed twice with 1 \times PBS, and 1 mL of assay buffer was added to the kit. The suspension was ultrasonicated for 20 min and centrifuged at 16,000 \times g for 15 min. After following the manufacturer's instructions, the standard and samples (n = 3 for each group) were incubated at 37 °C for 1 h. Absorbance at OD 593 nm was measured using a modular multimode microplate reader (BioTek Synergy H1).

2.10. Identifying nitroxoline target homologues in *A. castellanii* proteome

In the Research Collaboratory for Structural Bioinformatics (RCSB) Protein Data Bank (PDB), two entries with nitroxoline as the structural ligand were identified: 3A18 (Gene: CTSB, UniProt ID: P07858) and 5Y1Y (Gene: BRD4, UniProt ID: O60885) (Burley et al., 2023; UniProt Consortium, 2023). To identify proteins homologous to these two known nitroxoline targets in *A. castellanii*, the complete proteome dataset for *A. castellanii* (Proteome ID: UP000011083) was retrieved from the UniProt proteome database (<https://www.uniprot.org/pr/oteomes/UP000011083>). Sequence alignment of CTSB and BRD4 against the *A. castellanii* proteome was performed using the Needleman–Wunsch algorithm with a BLOSUM62 scoring matrix (Needleman and Wunsch, 1970). Proteins with a sequence similarity \geq 30% were considered potential nitroxoline targets within the *A. castellanii* proteome, with the highest similarity observed at 38% between proteins P07858 and L8H210.

2.11. Homology modelling and molecular docking

Homology modelling and molecular docking were conducted using Schrödinger Suite 2022–3 (New York, NY, USA). Proteins and ligands were prepared using the Protein Preparation Wizard and LigPrep modules in the Schrödinger Suite with default settings. A receptor grid was generated using the Receptor Grid Generation module in Schrödinger Suite, and the ligand diameter midpoint boxes were defined as 10 \times 10 \times 10 Å³. Molecular docking was performed using the Ligand Docking module in the Schrödinger Suite with SP precision, a flexible ligand sampling strategy, and a van der Waals radii scaling factor of 0.5 for the receptor and ligand (Friesner et al., 2006). Subsequently, docking poses underwent Prime MM-GBSA computation, where residues within 6 Å of the docked ligands were relaxed using the minimise sampling method. Finally, the binding free energies (MM-GBSA dG Bind) and chemotype diversity were calculated by visually inspecting the optimised docking pose and considering the SP docking scores.

2.12. Monodansylcadaverine (MDC) autophagy staining assay in trophozoites

An MDC staining assay kit (Beyotime, C3018S, Nanjing, China) was used to detect autophagic vesicles in autophagic cells. All vacuoles in the trophozoites were visualised using MDC staining. Following the manufacturer's instructions, trophozoites (1 \times 10⁵) after a 12-h treatment were washed once with 1 \times PBS and incubated for 30 min at 26 °C in 1 mL of assay buffer containing 1 μ L of MDC, the tracer of acidic autophagic vesicles. After three washes with assay buffer, fluorescent MDC signal acquisition (λ Ex = 335 nm and λ Em = 512 nm) was performed on a modular multimode microplate reader (BioTek Synergy H1).

2.13. Statistical analysis

All statistical analyses were performed using the GraphPad Prism 8 software (GraphPad Software, Version 8.0; San Diego, CA, USA). Comparisons between the control and treatment groups were performed using a one-way analysis of variance. Data are presented as means \pm standard deviation (SD), derived from \geq 3 independent experiments for each sample. Statistical significance was set at $p < 0.05$.

3. Results

3.1. Cell viability inhibition and morphology changes in *A. castellanii* after treatment with nitroxoline

To assess the in vitro efficacy of nitroxoline, we used the CellTiter-

Glo® Luminescent cell viability assay. The determined IC₅₀ value is presented in Fig. 1A, indicating that nitroxoline effectively inhibited *A. castellanii* trophozoites at 24 h with an IC₅₀ ≤ 16.08±0.93 μM. Fig. 1B depicts the time- and dose-dependent decreases in *A. castellanii* trophozoite viability in response to nitroxoline. Treatment with 20, 40, 60, and 80 μM of nitroxoline separately led to significant reductions in

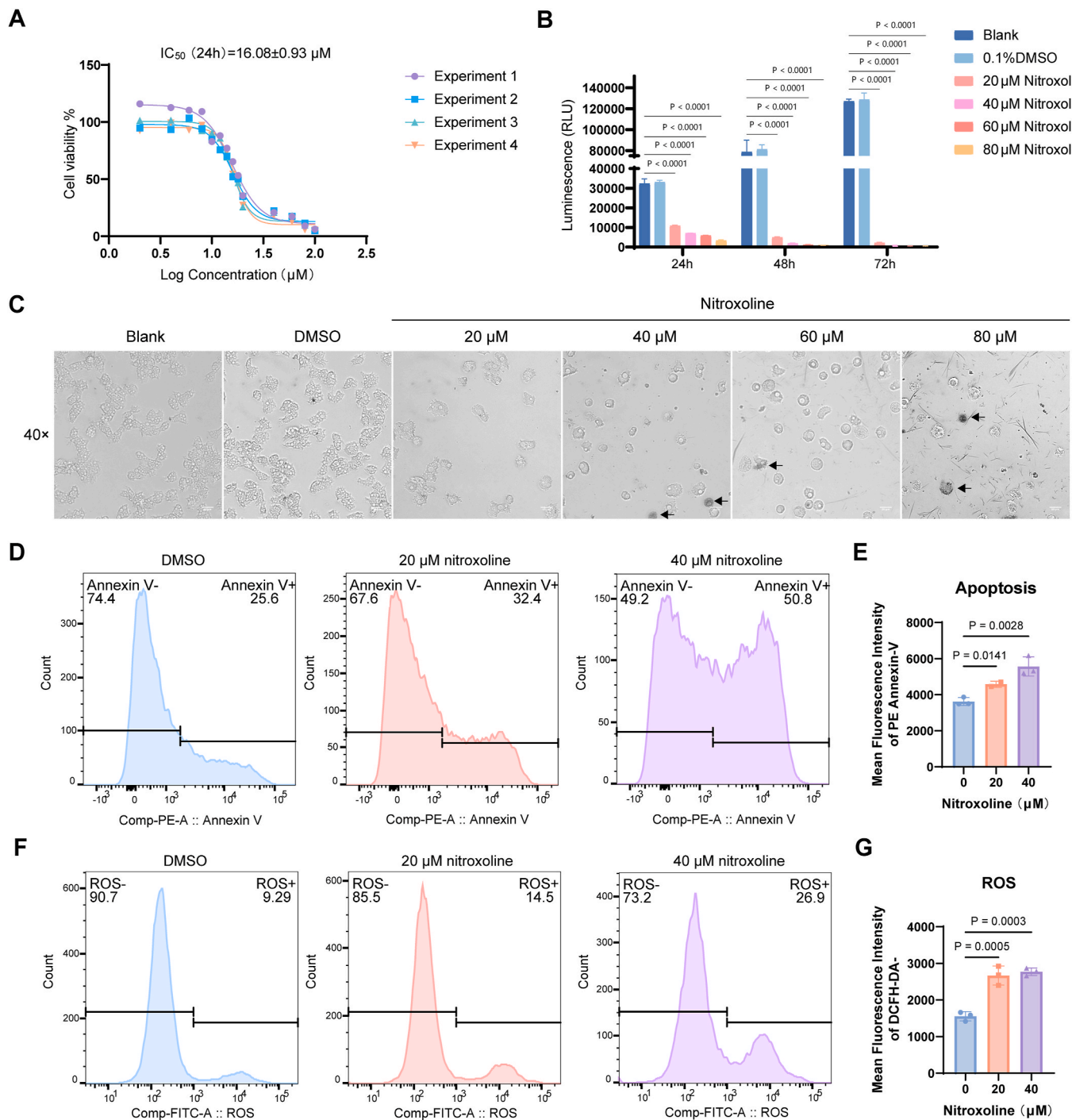


Fig. 1. Suppressing *A. castellanii* trophozoites viability by nitroxoline. (A) IC₅₀ values of nitroxoline-treated *A. castellanii* trophozoites determined by 24 h CellTiter-Glo assay. (B) Viability of trophozoites following 20–80 μM nitroxoline treatments for 24, 48, and 72 h determined using the CellTiter-Glo assay. Data are presented as means ± SDs from three experiments. Blank: without any treatments. DMSO-treated trophozoites (0.1%) were used as the negative control. (C) Effects on *A. castellanii* trophozoites incubated with negative control (0.1% DMSO) and different concentration of nitroxoline for 24 h monitored under an inverted microscope (magnification, × 40). Scale bar: 20 μm. The arrows indicate the solidified trophozoites treated with nitroxoline. (D) Trophozoites were treated with the indicated compound concentrations for 24 h. Apoptosis rate was measured using PE Annexin-V flow cytometry. (E) Mean fluorescence intensity of PE Annexin-V in each group. Data are presented as means ± SDs of three experiments. (F) Reactive oxygen species level was measured using DCFH-DA flow cytometry. (G) Mean fluorescence intensity of DCFH-DA in each group. Data are represented as means ± SDs of three separate experiments. SDs, Standard deviations.

trophozoite viability to $32.14\% \pm 0.97\%$, $20.87\% \pm 0.22\%$, $17.29\% \pm 0.70\%$, and $9.85\% \pm 0.93\%$ after 24 h ($p < 0.05$; Fig. 1B), respectively, compared with the 0.1% DMSO-treated group. Specifically, significant declines were observed at 20, 40, 60, and 80 μM of nitroxoline after 48 h ($6.35\% \pm 0.48\%$, $2.42\% \pm 0.27\%$, $1.51\% \pm 0.10\%$, and $1.15\% \pm 0.04\%$) and 72 h ($1.77\% \pm 0.26\%$, $0.55\% \pm 0.21\%$, $0.41\% \pm 0.02\%$, and $0.37\% \pm 0.06\%$) ($p < 0.05$; Fig. 1B). Data are presented as mean \pm SD from triplicate experiments.

Observation using an inverted microscope showed that the shape of the trophozoites was severely disrupted, and the boundary was blurred with increasing drug concentrations after 24 h (Fig. 1C). Trophozoites progressively became rounded and elliptical with spinous protrusions, and intracellular vacuoles disappeared and clustered together after 48 and 72 h of treatment (Fig. S1A). To investigate the effect of nitroxoline on the cyst stage, cysts were treated with 20 μM and 40 μM nitroxoline for 3 days and continued the observation for another 9 days. Trophozoites emerged in the 0.1% DMSO-treated groups on the third day, and appeared in the 20 μM nitroxoline-treated groups 3 days after the replacement of fresh medium, while no trophozoites were observed in the 40 μM nitroxoline-treated groups during the 12-day observation period (Fig. S1B).

To investigate whether nitroxoline-induced inhibition of trophozoite

viability was linked to apoptosis, we evaluated phosphatidylserine levels on apoptotic trophozoite membranes using Annexin V apoptosis detection. Flow cytometry analysis indicated that, compared with the control group, nitroxoline treatment significantly promoted cell apoptosis (Fig. 1D to E). Excessive accumulation of ROS can break cellular homeostasis, leading to oxidative stress (Liu et al., 2023). ROS determined using DCFH-DA increased in the nitroxoline-treated groups compared with the normal-cultured group (Fig. 1F to G). Nitroxoline treatment significantly decreased the MMP, indicating mitochondrial dysfunction (Fig. S2).

Collectively, these in vitro experiments demonstrate the inhibitory effect of nitroxoline on *A. castellanii* trophozoite growth.

3.2. General property and GO term enrichment analysis of transcriptome sequencing

Three parallel samples, separately from normal-cultured, DMSO-treated, 20 μM nitroxoline-treated, and 40 μM nitroxoline-treated groups after 24 h, respectively, were successfully subjected to RNA-seq (Fig. S3A). A principal component analysis plot further revealed distinctions among the four trophozoite groups (Fig. S3B). The expression profiles of the normal culture and DMSO-treated groups showed

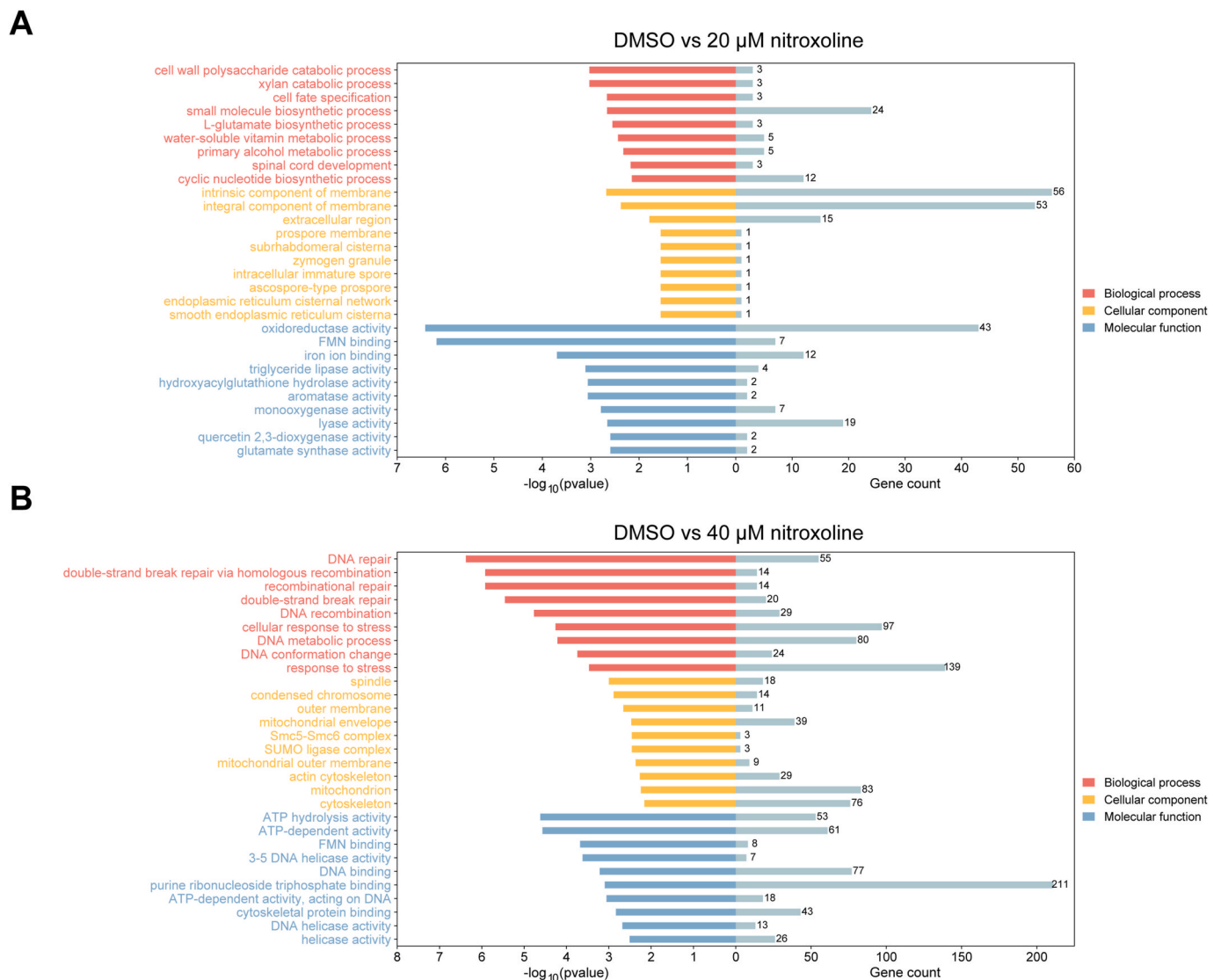


Fig. 2. GO analysis to characterise functional pathways in *A. castellanii* trophozoites affected by nitroxoline. (A, B) Bar plot of top GO terms for significantly changed genes in 20 (A) and 40 μM nitroxoline-treated trophozoites (B). Red: biological process (BP). Yellow: cellular component (CC). Blue: molecular function (MF).

minimal differences. The gene expression patterns from the 20 μ M nitroloxine-treated and 40 μ M nitroloxine-treated groups were discrete compared with the other groups (Fig. S3C), suggesting high variability of the expression profiles in nitroloxine-treated groups and indicating that many of the key variations in the genes in the expression profiles probably determined the drug efficacy to trophozoites. Volcano plots were also shown in which the blue and purple regions represent upregulated and downregulated genes with significant changes in differential abundance ($\log_2FC < -1$ or $\log_2FC > 1$; $p < 0.05$ based on Student's t-test with false discovery rate correction) (Figs. S3D–E).

To categorise the DEGs, GO term enrichment analysis was performed, which included three fundamental groups: biological processes (BP), cellular components (CC), and molecular functions (MF). BP analysis in the 20 μ M nitroloxine-treated group indicated that regulated DEGs were predominantly involved in the cell wall macromolecule catabolic process (Fig. 2A). Meanwhile, the significantly regulated DEGs in the CC category (Fig. 2A) were associated with components such as the intrinsic component of the membrane and integral component of the membrane. MF analysis (Fig. 2A) of 20 μ M nitroloxine-treated DEGs revealed enrichment in oxidoreductase activity, FMN binding, iron ion binding, triglyceride lipase activity, and hydroxyacyl glutathione

hydrolase activity. Nevertheless, in the 40 μ M nitroloxine-treated group, BP analysis (Fig. 2B) revealed significant alterations in a multitude of genes related to cellular response to DNA damage stimulus, DNA repair, and double-strand break repair via homologous recombination. In the CC category (Fig. 2B), components such as spindles, condensed chromosomes, outer membranes, mitochondrial envelope, and smc5-smc6 complex were distinctly clustered. In the MF analysis, DEGs were enriched in ATP hydrolysis activity, ATP-dependent activity, FMN binding, 3–5 DNA helicase activity, and DNA binding.

3.3. GO interaction network and KEGG pathway analysis

As depicted in the GO enrichment network, iron ion binding (GO:0005506) and oxidoreductase activity (GO:0016491) were enriched in the 20 μ M nitroloxine-treated group (Fig. 3A), and cellular response to DNA damage stimulus (GO:0006974) was the top cluster of enrichment in the 40 μ M nitroloxine-treated group (Fig. 3B). Pathway enrichment analysis based on KEGG terms revealed significant enrichment of regulated genes in hypertrophic cardiomyopathy; metabolic pathways; pyruvate metabolism; and fatty acid biosynthesis in the 20 μ M nitroloxine-treated group (Fig. 3C). Nonetheless, the genes in the 40

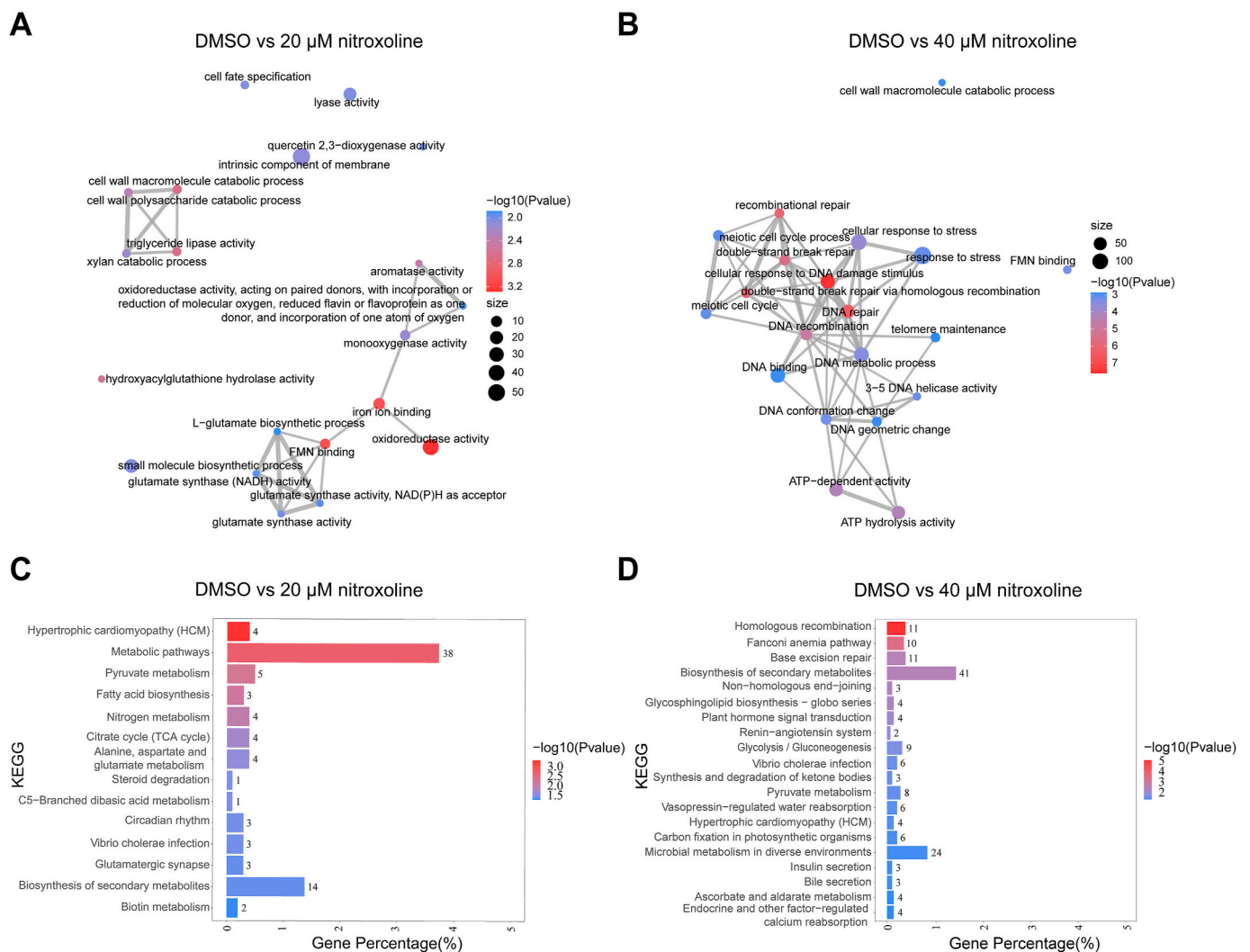


Fig. 3. Network diagrams and KEGG analysis in *A. castellanii* trophozoites affected by nitroloxine. (A, B) Network diagrams depict the top 20 Gene Ontology terms interactions, grouped by pathways. Line thickness corresponds to the number of shared genes between two pathways. The ratio of overlapping genes to unique genes is $\geq 20\%$. The colour and size of the circles indicate the value of significantly regulated genes among each cluster. (C, D) Bar plot of top enriched KEGG terms for significantly changed genes in 20 and 40 μ M nitroloxine-treated trophozoites. Statistical significance and gene percentage (number of genes in transcriptomic data versus all genes annotated with the KEGG term) are shown. KEGG, Kyoto Encyclopedia of Genes and Genomes.

μM nitroxoline-treated group were significantly enriched in homologous recombination, Fanconi anaemia pathway, base excision repair, biosynthesis of secondary metabolites, and non-homologous end-joining (Fig. 3D). Pathway enrichment analysis based on the GO interaction network and KEGG terms revealed significant enrichment of altered genes in various metabolic and DNA damage response (DDR) pathways. This transcriptomic response discrepancy to nitroxoline suggests that trophozoites adopt diverse regulatory mechanisms to counter external stress.

3.4. Nitroxoline alters the mRNA expression of trophozoites

The volcano plot showed that several DNA damage repair genes were upregulated after 24 h of treatment with nitroxoline (Fig. 4A to B), including *TOP2*, *PARG*, *BRCA2*, *FEN1*, and *RAD51*. In addition, several other DNA damage repair genes with significant upregulation following a 40 μM nitroxoline treatment of trophozoites were also observed (Fig. 4B), including *ATR*, *ATM*, *RAD50*, *RAD51 homolog*, *RAD54*, *RAD52*, *APE1*, *HDAC1*, *PARP149970* (UniProt IDs: L8HC40), *PARP256450* (UniProt IDs: L8GH34), *PARP114300* (UniProt IDs: L8H6I0), and *PARP338640* (UniProt IDs: L8HHX0). Upon further analysis of down-regulated genes following 40 μM nitroxoline treatment, the following genes were altered in trophozoites: *SAHH*, *GNMT*, *CBS*, *Cys1a*, and *MAT*. Genes (UniProt IDs: L8GGB2, L8GKJ9) belonging to the cytochrome p450 superfamily were upregulated in 20 μM and 40 μM nitroxoline treatments.

Visualising the selected DEGs within these pathways using a heatmap (Fig. 4C) revealed distinct gene expression patterns. Nitroxoline can positively or negatively affect metabolic enzymes. Treatment with 40 μM nitroxoline impacted methionine and cysteine cycles by decreasing the expression of *GNMT*, *SAHH*, *CBS*, and *Cys1a* (Fig. 4C) and increasing the expression of *BHMT* (Figs. S4A–B) in *A. castellanii*. In addition to the rescue of cell proliferation upon cysteine deprivation, *GNMT* expression normalised cellular oxidative stress, and the transsulfuration pathway is required to sustain glutathione levels and redox balance in vivo (Zhu et al., 2019). Therefore, the loss of *GNMT* and *CBS* may disturb cellular oxidative homeostasis. Nevertheless, nitroxoline significantly activated various kinases, such as *ATM* and *ATR*, which act as the primary transducers in the DDR signalling cascade (Fig. 4C). Many of the downstream genes involved in DNA damage, such as *PARP*, *PARG*, *MRE11*, *RAD50*, *RAD51*, and *APE1*, exhibited high expression levels after 40 μM nitroxoline treatment (Fig. 4C). As the major contributors to detecting DNA damage and maintaining genomic stability, *HDAC1* showed increased expression in the 40 μM nitroxoline-treated group. Consequently, several physiologically important antioxidant enzymes of the peroxiredoxin, thioredoxin, and glutathione systems, such as *PRX*, *PRX2*, *TRX*, *TrxR*, *GSR*, and *HYR1*, were significantly upregulated in the 20 and 40 μM nitroxoline-treated groups (Fig. 4C). *ATG8*, *ATG9*, *ATG16L2* and *ATG27*, the autophagy-related genes, represented high mRNA expression levels after 40 μM nitroxoline treatment (Fig. 4C).

To further verify the consistency of the transcriptome results, RT-PCR was performed. The expression of the vital metabolic pathway genes *SAHH*, *GNMT*, and *CBS* exhibited significant downregulation after 20 and 40 μM nitroxoline treatment. In contrast, a significant increase in the redox system genes *GSR* and *TRX* and the DNA damage repair-related genes *ATM*, *ATR*, *RAD51*, and *FEN1* (Fig. 4D) were revealed in the 20 and 40 μM nitroxoline-treated groups. The expression of the other DNA repair relative genes *APE1*, *DNA2*, *PARP*, *PARG*, *MRE11*, and *RAD50* (Figs. S4C–H) increased only after 40 μM nitroxoline treatment, consistent with the transcriptomics. *DMT1*, involved in iron acquisition, was also upregulated in the 20 and 40 μM nitroxoline-treated groups (Fig. 4D). The autophagy-related genes *ATG8*, *ATG9*, and *ATG16* were significantly upregulated after 24 h of exposure to 20 or 40 μM nitroxoline (Fig. 4D), while *ATG27* remained relatively changed only after 40 μM nitroxoline treatment. Compared with the control group, only trophozoites treated with 40 μM nitroxoline showed more accumulation

of autophagic vacuoles (Fig. S4I), consistent with the expression of autophagy-related genes. Moreover, the number of apurinic/apyrimidinic sites in DNA increased in the nitroxoline-treated groups, indicating probable nitroxoline-induced DNA damage (Fig. 4G).

3.5. Nitroxoline reduces the H₂S production of trophozoites

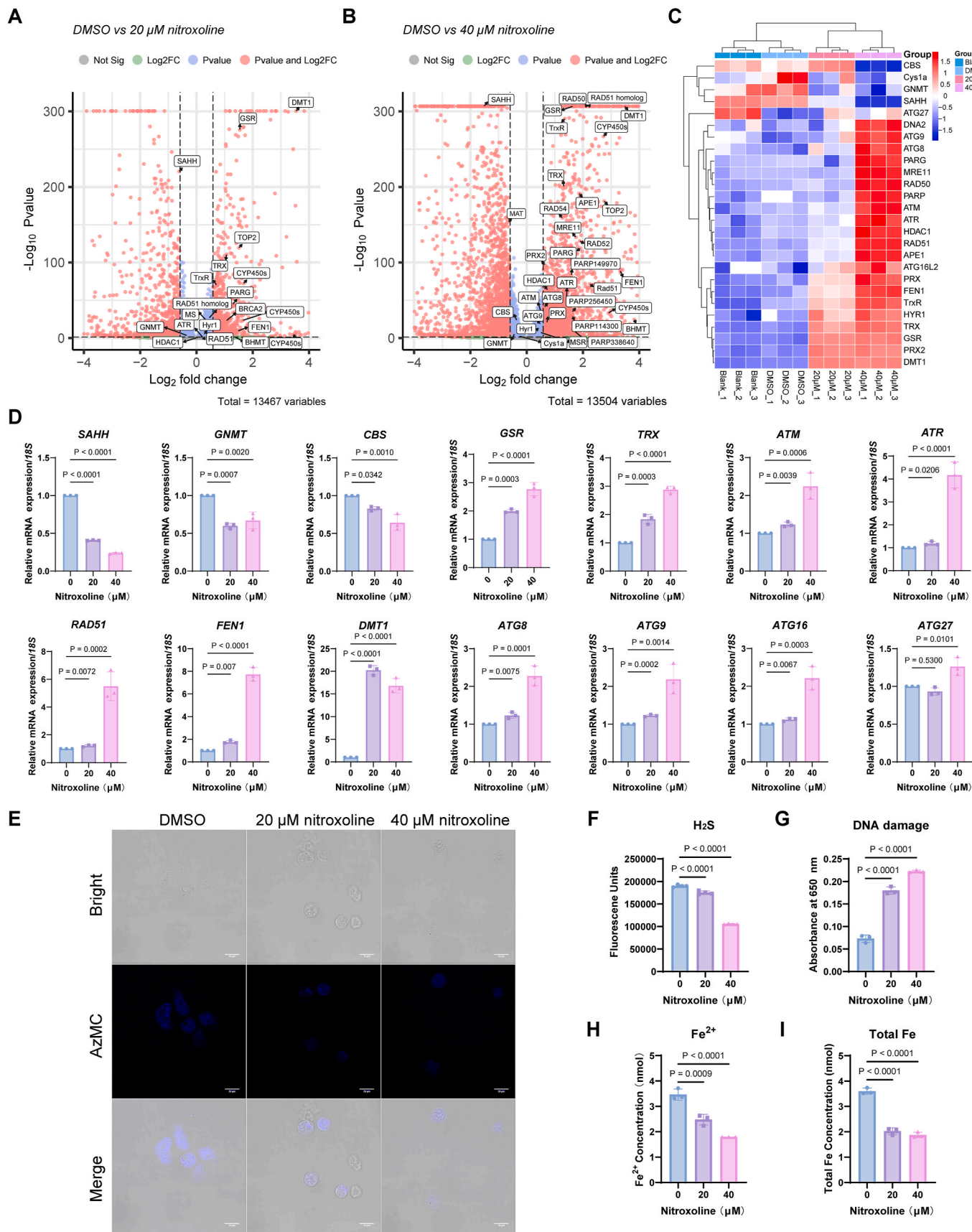
8-Hydroxyquinoline derivatives can decrease the activity of *CBS* (Conan et al., 2022). *CBS* encodes a pyridoxal 5'-phosphate-dependent enzyme that catalyses the condensation of homocysteine and serine to form cystathionine, which is a branch of the transsulfuration pathway. The transsulfuration pathway is the primary route for the biosynthesis of the major cellular antioxidants cysteine and glutathione, and cystathionine and its downstream partner *CBS* produce the gaseous transmitter H₂S, another ROS scavenger, as a byproduct of their enzymatic activity (Garcia et al., 2023). Since *CBS* is also involved in H₂S production, we measured its levels using an AzMC fluorogenic probe (Hu et al., 2019). To investigate the effects of nitroxoline on trophozoites, H₂S fluorescence imaging was performed using an AzMC probe (Fig. 4E). A 24-h treatment with 20 μM or 40 μM of nitroxoline significantly decreased H₂S production levels by $7.90\% \pm 2.82\%$ and $44.54\% \pm 0.82\%$, respectively, compared with the control group (Fig. 4F). Notably, nitroxoline reduced the level of endogenous H₂S in a dose-dependent manner. Nitroxoline reduced H₂S production in cellular lysates, revealing a possible effect on regulating *CBS* expression levels or protein stability, which is similar to the above results showing that the mRNA expression level of *CBS* was significantly decreased after nitroxoline treatment for 24 h (Fig. 4D).

3.6. Nitroxoline impacts iron uptake transcripts in trophozoites

A previous study postulated that nitroxoline induces rapid iron starvation in the biofilms of several important pathogens (Liu et al., 2022). We were curious whether nitroxoline could affect iron uptake in *A. castellanii* trophozoites. Full transcriptomic analysis of nitroxoline-treated trophozoites revealed that the iron ion-binding pathways (Fig. 3A) were significantly affected. Nitroxoline treatment increased the transcription of genes involved in iron acquisition, including divalent metal transporter 1 (*DMT1*) (Fig. 4C to D). Bioinformatic analysis showed that *A. castellanii* genomes encode one gene product with homology to *Plasmodium falciparum* PfDMT1, *Arabidopsis thaliana* NRAMP2, and *Homo sapiens* DMT1 (NRAMP2). The *DMT1* homolog was *ACA1_225890* in *A. castellanii* (AcDMT1), which shared 58.31% amino acid sequence identity with *A. thaliana* NRAMP2, 56.67% with *H. sapiens* DMT1, and 28.38% with *P. falciparum* PfDMT1 (Table S2). *DMT1* is essential for maintaining iron homeostasis and enables Fe²⁺ and Mn²⁺ ion entry into the mitochondria. Therefore, *DMT1* promotes mitochondrial heme synthesis, iron-sulphur cluster biogenesis, and antioxidant defence (Wolff et al., 2014). The intracellular iron levels in nitroxoline-treated trophozoites were also confirmed (Fig. 4H to I). As depicted above, nitroxoline, especially at 40 μM , significantly decreased intracellular Fe²⁺ and total Fe amounts in trophozoites compared with the control group. These results establish a structural basis for the pharmacological intervention of nitroxoline on trophozoites.

3.7. Searching potential targets of nitroxoline in *A. castellanii* proteome

By searching ligand 'Nitroxoline' in the RCSB PDB database, two entries (PDB codes: 3AI8 and 5Y1Y) were found with nitroxoline as a structural ligand. The first entry was human Cathepsin B (gene: *CTSB*, UniProt ID: P07858), which belongs to a family of lysosomal cysteine proteases known as cysteine cathepsins and plays an important role in intracellular proteolysis. The latter belongs to the human BET family of BRD4 (UniProt ID: O60885), a chromatin reader protein that recognises and binds to acetylated histones and plays a key role in transmitting



(caption on next page)

Fig. 4. Transcript profiles in trophozoites treated with nitroxoline. (A, B) Enhanced volcano plot of the DEGs in trophozoites under 20 and 40 μM nitroxoline treatments, respectively. The metabolic pathways, DNA damage repair pathway and mitochondrial function related genes significant ($|\text{Fold change}| \geq 1.5$, P value ≤ 0.05) are annotated. (C) Heat map of DEGs in nitroxoline-treated groups compared with DMSO-treated and normal-cultured groups (Blank). Increased and decreased abundances, relative to the control, are shown in red and blue, respectively. (D) Relative mRNA expression of *SAHH*, *GNMT*, *CBS*, *GSR*, *TRX*, *ATM*, *ATR*, *RAD51*, *FEN1*, *DMT1*, *ATG8*, *ATG9*, *ATG16*, and *ATG27* under 20 and 40 μM nitroxoline treatments for 24 h in *A. castellanii* trophozoites. Gene expression was normalised to *18S* expression levels. Results represent means \pm standard deviations of three independent experiments. (E) Representative H_2S live-cell fluorescence images after treatment of nitroxoline. Trophozoites were pre-treated and stained with 100 μM AzMC for 1 h. Scale bars, 20 μm . (F) Endogenous levels of H_2S were detected using AzMC fluorescence assays ($\lambda_{\text{Ex}} = 365 \text{ nm}$, $\lambda_{\text{Em}} = 450 \text{ nm}$). (G) DNA damage was assessed using avidin-biotin assays ($\text{OD} = 650 \text{ nm}$) (H, I) Iron amount (Fe^{2+} and Fe^{3+}) was monitored using absorbance assays ($\text{OD} = 593 \text{ nm}$). DEGs, Differentially expressed genes; OD, Optical density.

epigenetic memory across cell divisions and transcription regulation. To identify possible *A. castellanii* proteins that are homologous to the known targets of nitroxoline (Cathepsin B and BRD4), we first downloaded the complete proteomic data of *A. castellanii* from the UniProt Proteomes database with 14,939 entries. The Needleman–Wunsch algorithm was used for sequence alignment using the BLOSUM62 scoring matrix. Cathepsin B and BRD4 sequences were globally aligned with all sequences in the *A. castellanii* proteome, followed by calculating sequence similarity. Unlike the high sequence similarity that exceeding 80–90% when comparing human proteins with those from closely

related mammals, the overall sequence similarity between human and several *A. castellanii* proteins is markedly lower, with the highest similarity observed at 38% between proteins P07858 and L8H210. A sequence similarity cutoff ($\geq 30\%$) was applied to isolate 639 homology proteins in *A. castellanii* (Table S3) that possibly as potential targets. In addition, by comparing the GO annotation data of 639 homologous proteins with the GO term enrichment analysis outcomes illustrated in Fig. 2A–C, 69 *A. castellanii* proteins overlapped to potentially bind nitroxoline and associate with the DEGs caused by nitroxoline treatment. Homology modelling and molecular docking were performed for

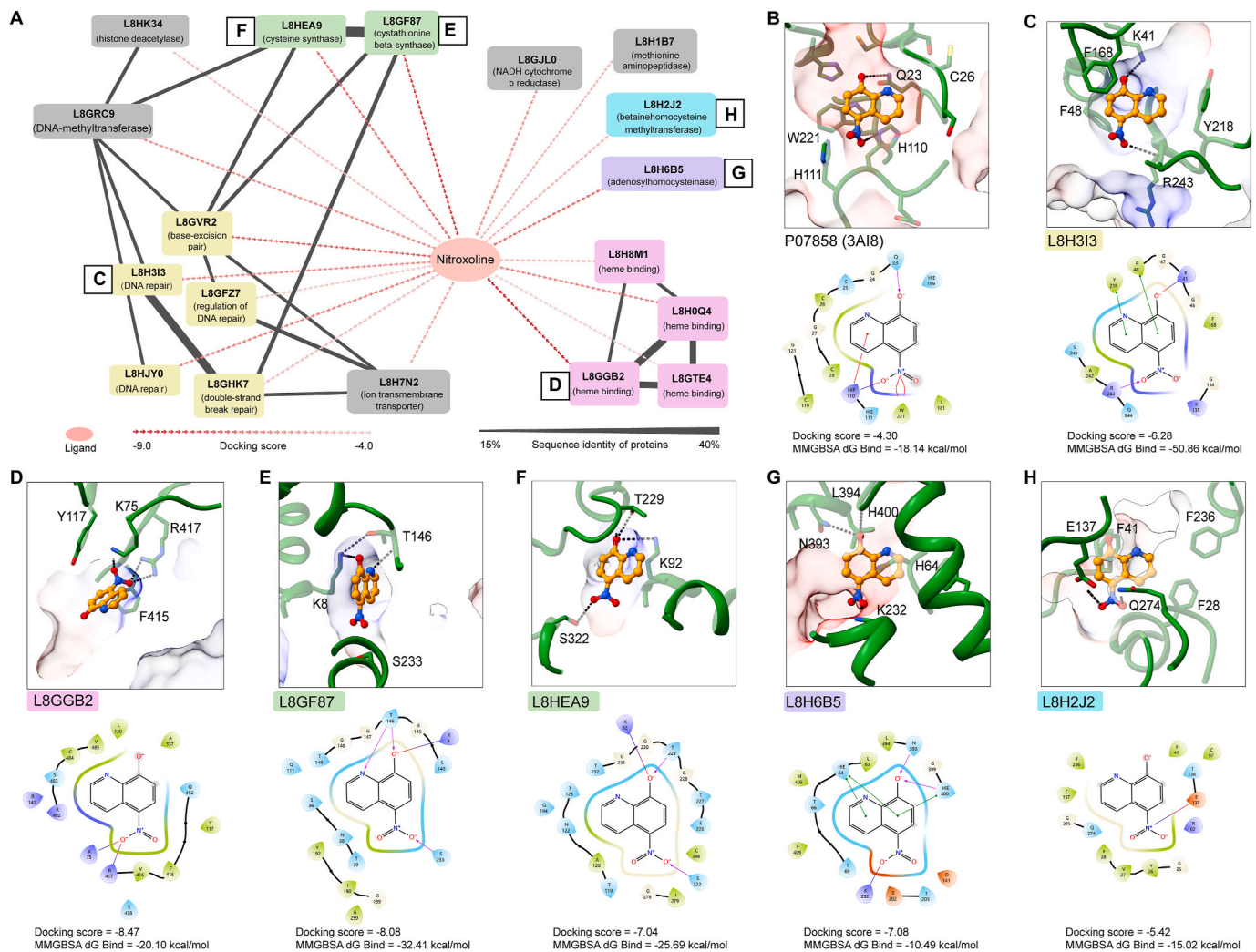


Fig. 5. Protein similarity network and docking poses of nitroxoline in the potential *A. castellanii* targets. (A) Interaction network of nitroxoline with potential *A. castellanii* targets. (B–H) The surface representation and two-dimensional diagrams illustrate ligand–protein interactions within the predicted nitroxoline-binding pockets of potential targets, including positive control (B), DNA repair protein RAD51 (C), cytochrome p450 (D), cystathionine beta-synthase (E), cysteine synthase (F), adenosylhomocysteinase (G), and betainehomocysteine methyltransferase (H). The colour coding transitions from dodger blue, representing the most hydrophilic regions, to orange to red, indicating the most hydrophobic regions, within the surface representation. Key residues implicated in recognising nitroxoline are depicted as sticks. Polar interactions are denoted by black dashed lines. The amino acids of potential target residues are highlighted to indicate positive charge (blue), negative charge (red), polar (cyan), and hydrophobicity (green).

these 69 proteins using the Schrödinger Suite 2022–3, allowing for conformational flexibility of the targets and nitroxoline. As a positive control, we redocked the complex structure of cathepsin B with nitroxoline (PDB ID: 3AI8), obtaining a docking scoring of -4.30 and binding free energy (MMGBSA dG Bind) of -18.14 (Fig. 5B, Table 1). After analysing the docking scores and binding poses, 18 proteins were identified as potential *A. castellanii* targets of nitroxoline (Fig. 5, Table 1).

The 18 potential targets were categorised into four groups. The first group included five proteins related to DNA repair that are crucial for protecting the genome from damage and mutations, thereby ensuring cell survival. The DNA repair protein RAD51 (UniProt ID: L8H3I3), which contains the Rad51 domain, had a good docking score of -6.28 and the best binding free energy (MMGBSA dG Bind) of -50.86 kcal/mol, significantly better than that of the control. Nitroxoline was stabilised through multiple stacking interactions with F48 and Y218 and polar interactions with K41 and K243 (Fig. 5C). The second group comprised four proteins belonging to the cytochrome p450 family, which play essential roles in detoxifying and eliminating various compounds, the synthesis and breakdown of hormones, cholesterol synthesis, and vitamin D metabolism. L8GGB2, which contains the P450 domain, had the best docking score of -8.47 and a binding free energy of -20.10 kcal/mol. Nitroxoline formed salt bridges with K75 and R417 and engaged in extensive hydrophobic interactions with the surrounding residues (Fig. 5D). The third group comprised two proteins (UniProt IDs: L8GF87 and L8HEA9) associated with cysteine synthesis. By sharing similar binding pockets, they primarily interact with nitroxoline through polar interactions (via K8/K92, T146/T229, and S233/S322) and display high docking scores and binding free energies (-8.08 and -7.04 ; MMGBSA dG Bind: -32.41 and -25.69 kcal/mol, respectively) (Fig. 5E to F). Additionally, seven discrete proteins were classified as others

Table 1

List of the potential nitroxoline targets in *A. castellanii* that also associated with the Gene Ontology analysed functional pathways in *A. castellanii* trophozoites affected by nitroxoline.

Group	Targets	Docking Score	MMGBSA dG Bind (kcal/mol)	Protein Names
Proteins associated with DNA repair	L8H3I3	-6.28	-50.86	DNA repair protein RAD51 homolog
	L8HJY0	-6.52	-25.29	DNA repair protein
	L8GFZ7	-4.82	-12.16	Tyrosyl-tRNA synthetase
	L8GVR2	-7.16	-1.33	Flap endonuclease
	L8GHK7	-5.12	0.28	Rad5111 protein
Cytochrome p450 family	L8H8M1	-5.21	-39.31	Cytochrome P450 monooxygenase, putative
	L8GGB2	-8.47	-20.10	Cytochrome p450 superfamily protein
	L8GTE4	-4.66	-6.48	Cytochrome P450, putative
	L8HOQ4	-6.48	8.02	Cytochrome p450 superfamily protein
Cysteine synthase related proteins	L8GF87	-8.08	-32.41	Cystathionine beta-synthase
	L8HEA9	-7.04	-25.69	Cysteine synthase
Others	L8GRC9	-6.25	-26.34	DNA (cytosine-5)-methyltransferase
	L8GJL0	-6.20	-16.38	NADH cytochrome b reductase, putative
	L8H2J2	-5.42	-15.02	Betainehomocysteine methyltransferase
	L8H6B5	-7.08	-10.49	Adenosylhomocysteinase
	L8H1B7	-5.48	-2.82	Methionine aminopeptidase
	L8H7N2	-5.74	-2.79	Uncharacterized protein
	L8HK34	-5.14	4.25	histone deacetylase
Control	P07858 (3AI8)	-4.30	-18.14	Cathepsin B

(Fig. 5A–Table 1). Among them, adenosylhomocysteinase (UniProt ID: L8H6B5) and betainehomocysteine methyltransferase (UniProt ID: L8H2J2) had relatively better docking scores with nitroxoline (-7.08 and -5.42), being stabilised through multiple stacking and polar interactions (Fig. 5G to H). Collectively, these bioinformatic analyses and molecular docking studies support the possibility of direct interactions between nitroxoline and several *A. castellanii* proteins.

4. Discussion

We elucidated the effects of nitroxoline on *A. castellanii* trophozoites in biological activities and molecular mechanisms, as illustrated in the schematic. Our assays against *A. castellanii* showed a IC_{50} value of $16.08 \pm 0.93 \mu M$ on acanthamoeba, slightly higher than that on *Naegleria fawcarii* trophozoites, about $1.63 \pm 0.37 \mu M$ in a previous study. And we also investigated the effects of nitroxoline on *A. castellanii* cyst stage. Methods for evaluating RNA expression levels, such as microarrays and RNA-seq, have become valuable tools for assessing the dynamic properties of biological systems in a fast, broad, and reliable manner. In addition to technological aspects, developing bioinformatic analytical methods and tools has enormously aided our capacity to extract knowledge from omics technologies.

Reactive oxygen and nitrogen species are unavoidable byproducts of metabolic and energy transfer processes in oxidative life. These molecules play pivotal roles in regulating cellular processes. However, excess amounts of ROS or reactive nitrogen species cause oxidative and nitrosative stress, which may damage macromolecules. Free radicals generated in cells under oxidative stress can directly attack cellular membranes. Nitroxoline increased intracellular ROS levels in a dose-dependent manner. Consistent with this idea, nitroxoline treatment significantly increased *GPX* and *GSR* expression, indicating strong intracellular oxidation modulation. Additionally, following the momentum of “big data” research, *Trx*, *TrxR*, and *MsrA* were strongly upregulated after exposure to nitroxoline. Furthermore, *A. castellanii TrxR-S* reduces *Trx-1*, which reduces *Prx-1* and *MsrA*, suggesting that the synergistic interactions of these antioxidant enzymes are integral to the response to oxidative stress (Leitsch et al., 2021). In a more recent study, mitochondrial fragmentation was accompanied by perturbations in energy production and elevated cellular ROS production (Aoyagi et al., 2022). In our study, nitroxoline significantly induced mitochondrial depolarisation in a dose-dependent manner.

Additional evidence for the role of nitroxoline in metabolic reprogramming comes from proteomic data in *E. coli*, highlighting the significant impact of this drug on metabolism (Deschner et al., 2024). When it comes to how nitroxoline impacted metabolic pathways, such as the methionine and cysteine cycles, the important clues come from the volcano plot of DEGs, which show the upregulated expression of *BHMT* and *MS* and downregulated expression of *GNMT*, *SAHH*, *CBS*, and *Cys1a*. The action of either *MS* or *BHMT* occurs during the resynthesis of methionine using homocysteine (HCY). *GNMT* plays an important role in methionine clearance (Johnson and Cuellar, 2023). The result of these changes is a potential increase in methionine synthesis. Methionine is a major target of ROS, and its metabolism signals a state of nutrient deprivation (Ouyang et al., 2020; Parkhitko et al., 2019). A myriad of studies have shown that excess methionine also induces the transcription of ribosomal and rRNA genes and overall translation capacity (Laxman et al., 2013). Cysteine can be converted from o-succinyl-L-serine by *Cys1a* and is also a product of the transsulfuration pathway and precursor for the synthesis of tripeptide γ -glutamyl cysteinyl glycine (glutathione) (Lampe et al., 2023; Salazar et al., 2022). Cysteine, homocysteine, glutathione, and cysteinyl glycine were the most abundant sulfhydryl groups. All these molecules are important in radical interactions as they are particularly susceptible to oxidation by ROS (Chondrogianni et al., 2014). Subsequently, we found intriguing alternatives that nitroxoline could impact the expression of *CBS*, which is the first rate-limiting step in the transsulfuration pathway (Zhu et al.,

2019). Additionally, we traced the effect of the reduction in CBS expression levels to its byproduct, H₂S, and its role as a gaseous transmitter or ROS scavenger within the cell (Parkhitko et al., 2019). Following this hypothesis, H₂S fluorescence imaging and qualitative analysis depicted nitroxoline substantially decreased the amount of H₂S in *A. castellanii* trophozoites. H₂S protects the cells from oxidative stress and modulates neuronal transmission, smooth muscle relaxation, insulin release, and inflammatory responses. In mammalian cells, endogenous H₂S is produced by three enzymes: CSE, CBS, and 3-MST (Parkhitko et al., 2019). However, CSE and 3-MST are not annotated in the *A. castellanii* database. Since all these metabolic pathways and genomic integrity safeguards play crucial roles in maintaining cellular homeostasis and are critical for growth, they are acutely sensed and trigger signalling responses. Autophagy is required for maintaining cellular homeostasis. Autophagy occurs when trophozoites face drug stress and subsequently, experience a degree of amino acid starvation. Therefore, whether nitroxoline could contribute to autophagy is conceivable. Genetic analyses have identified that several autophagy-related genes (such as *ATG8*, *ATG9*, *ATG16* and *ATG27*) that execute and regulate autophagy were significantly upregulated. ATGs are organised into functional complexes that participate in each step of macroautophagy. Upregulating autophagy genes have also been observed in flies lacking *GNMT* (Tain et al., 2020). An imbalance in HCY, glutathione, and cysteine metabolism can modulate autophagy (Desideri et al., 2012; Paul et al., 2018; Wang et al., 2019). In our study, nitroxoline significantly decreased the expression of *GNMT* and *CBS*, indicating a potential relationship between autophagy and metabolic pathways. Cellular oxidative stress is also key to autophagic response modulation (Ouyang et al., 2020). Eventually, after prolonged exposure to nitroxoline, the trophozoites transitioned from autophagy to apoptosis.

Nitroxoline can cause DNA damage in trophozoites at high concentrations, which is consistent with the upregulated mRNA expression of an arsenal of enzymes capable of sensing replication stress and transducing information to influence cellular responses and neutralise the destructive effects of aberrant DNA structures. Transcriptomic and qPCR analyses showed the upregulation of *ATM*, *ATR*, *RAD51*, *RAD50*, *MRE11*, and *FEN1*. The DNA damage repair is a complex signal transduction pathway (X. Zhang et al., 2023). The first step in DSBs (DNA double-strand breaks) is recruiting repair factors at DNA break sites, which are initially recognised by the MRE11-RAD50-NBS1 complex and promote ATM activation and DNA preparation for HR (McCarthy-Leo et al., 2022; Menolfi and Zha, 2020). RAD51, a key protein that corrects errors in replication forks, is a canonical marker of DNA damage (Ciccio and Elledge, 2010; Paulet et al., 2022). Volcano analysis also revealed several significant PARPs, including UniProt IDs: L8HC40, L8GH34, L8H610, and L8HHX0. PARP is a cellular stress sensor that is activated by oxidative, metabolic, and genotoxic stresses, such as single-strand break repair and double-strand DNA breaks, and in response, directs cells to specific fates according to the type and strength of the stress stimulus.

Homology modelling and molecular docking were performed to identify the potential targets of nitroxoline. Four main groups were categorised: five proteins related to DNA repair, four belonging to the cytochrome p450 family, two associated genes with cysteine synthesis, and seven classified as others. The DNA repair protein RAD51 (UniProt IDs: L8H3I3), which contains the Rad51 domain, had a good docking score of -6.28 and the best binding free energy (MMGBSA dG Bind) of -50.86 kcal/mol. Cys1a (UniProt IDs: L8HEA9) and CBS (UniProt IDs: L8GF87) shared similar binding pockets, primarily interacted with nitroxoline through polar interactions (via K8/K92, T146/T229, and S233/S322), and displayed high docking scores and binding free energies. SAHH (UniProt ID: L8H6B5) and BHMT (UniProt ID: L8H2J2) had relatively better docking scores with nitroxoline (-7.08 and -5.42), being stabilised through multiple stacking and polar interactions. Collectively, these transcriptomic analyses and molecular docking studies supported the possibility of direct interactions between

nitroxoline and several *A. castellanii* proteins.

Previous studies suggested that nitroxoline exerts its antibacterial effects by chelating metal ions such as Fe²⁺, Mn²⁺, Mg²⁺, and Ca²⁺ (He et al., 2024; Pelletier et al., 1995). Iron and copper are transition metal ions that can cleave hydroperoxides to form radicals that initiate chain reactions (Chondrogianni et al., 2014). Our findings suggest that the intracellular iron levels (Fe²⁺ and Fe³⁺) of nitroxoline-treated trophozoites were significantly decreased, and the transcription of *DMT1* (UniProt IDs: L8H7N2), which is involved in iron acquisition, was increased. The *A. castellanii* genome encodes a gene with homology to *Plasmodium falciparum* PfDMT1, *Arabidopsis thaliana* NRAMP2, and *Homo sapiens* DMT1 (NRAMP2). The DMT1 homolog is AcDMT1, which shares 58.31% amino acid sequence identity with *A. thaliana* NRAMP2, 56.67% with *H. sapiens* DMT1, and 28.38% with *P. falciparum* PfDMT1. The observed increase in the expression of intracellular ferrous iron transporters suggests a potential increase in intracellular recycling or the liberation of stored iron, aiding in sustaining growth within these comparatively brief timeframes (Lampe et al., 2023). Furthermore, the regulatory mechanisms underlying the changes in iron metabolism remain unclear. Further studies are underway to test these hypotheses.

Putting these nascent studies together, an early mechanistic picture began to coalesce that nitroxoline could impact the viability of *A. castellanii* trophozoites in a dose- and time-dependent manner, with increased metabolic process disorders, intracellular ROS production, DNA damage, iron starvation, decreased endogenous H₂S, decreased mitochondrial outer membrane permeabilisation, and the possibility of direct interactions between nitroxoline and several *A. castellanii* proteins.

CRediT authorship contribution statement

Lijun Chen: Writing – original draft, Software, Methodology, Investigation. **Wei Han:** Software, Methodology. **Wenwen Jing:** Writing – review & editing, Methodology. **Meng Feng:** Writing – review & editing, Methodology. **Qingtong Zhou:** Writing – review & editing, Software, Methodology, Funding acquisition, Conceptualization. **Xunjia Cheng:** Writing – review & editing, Funding acquisition, Conceptualization.

Data availability

The original contributions of this study are included in the article/supplementary material section.

Ethics approval

Not applicable.

Funding

This work was supported by the National Natural Science Foundation of China 81572020 and 82372278 (XC), STI2030-Major Project 2021ZD0203400 (QZ), and Hainan Provincial Major Science and Technology Project ZDKJ2021028 (QZ).

Declaration of competing interest

The authors declared no conflict of interest.

Acknowledgments

We thank Shuhui Sun and Shanghai NewCore Biotechnology Co., Ltd. (<https://www.bioinformatics.com.cn>, last accessed on Nov 10, 2023) for technical assistance.

Appendix A. Supplementary data

Supplementary data to this article can be found online at <https://doi.org/10.1016/j.ijpddr.2025.100578>.

References

- Aoyagi, Y., Hayashi, Y., Harada, Y., Choi, K., Matsunuma, N., Sadato, D., Maemoto, Y., Ito, A., Yanagi, S., Starczynowski, D.T., Harada, H., 2022. Mitochondrial fragmentation triggers ineffective hematopoiesis in myelodysplastic syndromes. *Cancer Discov.* 12, 250–269. <https://doi.org/10.1158/2159-8290.CD-21-0032>.
- Bojkova, D., Zöller, N., Tietgen, M., Steinhilber, K., Bechtel, M., Rothenburger, T., Kandler, J.D., Schneider, J., Corman, V.M., Ciesek, S., Rabenau, H.F., Wass, M.N., Kippenberger, S., Göttig, S., Michaelis, M., Cinatl, J., 2023. Repurposing of the antibiotic nitroxoline for the treatment of mpox. *J. Med. Virol.* 95, e28652. <https://doi.org/10.1002/jmv.28652>.
- Burley, S.K., Bhikadiya, C., Bi, C., Bittrich, S., Chao, H., Chen, L., Craig, P.A., Crichlow, G. V., Dalenberg, K., Duarte, J.M., Dutta, S., Fayazi, M., Feng, Z., Flatt, J.W., Ganesan, S., Ghosh, S., Goodsell, D.S., Green, R.K., Guranovic, V., Henry, J., Hudson, B.P., Khokhriakov, I., Lawson, C.L., Liang, Y., Lowe, R., Peisach, E., Persikova, I., Piehl, D.W., Rose, Y., Sali, A., Segura, J., Sekharan, M., Shao, C., Vallat, B., Voigt, M., Webb, B., Westbrook, J.D., Whetstone, S., Young, J.Y., Zalevsky, A., Zardecky, C., 2023. RCSB Protein Data Bank (RCSB.org): delivery of experimentally-determined PDB structures alongside one million computed structure models of proteins from artificial intelligence/machine learning. *Nucleic Acids Res.* 51, D488–D508. <https://doi.org/10.1093/nar/gkac1077>.
- Cabrera-Aguas, M., Khoo, P., Watson, S.L., 2022. Infectious keratitis: a review. *Clin. Exp. Ophthalmol.* 50, 543–562. <https://doi.org/10.1111/ceo.14113>.
- Chen, L., Han, W., Jing, W., Feng, M., Zhou, K., Cheng, X., 2024. Novel anti-Acanthamoeba effects elicited by a repurposed poly (ADP-ribose) polymerase inhibitor AZ9482. *Front. Cell. Infect. Microbiol.* 14, 1414135. <https://doi.org/10.3389/fcimb.2024.1414135>.
- Chondrogianni, N., Petropoulos, I., Grimm, S., Georgila, K., Catalgol, B., Friguet, B., Grune, T., Gonos, E.S., 2014. Protein damage, repair and proteolysis. *Mol. Aspect. Med.* 35, 1–71. <https://doi.org/10.1016/j.mam.2012.09.001>.
- Ciccia, A., Elledge, S.J., 2010. The DNA damage response: making it safe to play with knives. *Mol. Cell* 40, 179–204. <https://doi.org/10.1016/j.molcel.2010.09.019>.
- Conan, P., Léon, A., Gourdel, M., Rollet, C., Chair, L., Caroff, N., Le Jossic-Corcos, C., Sinane, M., Gentile, L., Maillebouis, L., Loaëc, N., Martin, J., Vilaire, M., Corcos, L., Mignen, O., Croyal, M., Voisset, C., Bihel, F., Friocourt, A.G., 2022. Identification of 8-hydroxyquinoline derivatives that decrease cystathionine beta synthase (CBS) activity. *Int. J. Mol. Sci.* 23, 6769. <https://doi.org/10.3390/ijms23126769>.
- Damhorst, G.L., Watts, A., Hernandez-Romieu, A., Mel, N., Palmore, M., Ali, I.K.M., Neill, S.G., Kalapala, A., Cope, J.R., 2022. Acanthamoeba castellanii encephalitis in a patient with AIDS: a case report and literature review. *Lancet Infect. Dis.* 22, e59–e65. [https://doi.org/10.1016/S1473-3099\(20\)30933-6](https://doi.org/10.1016/S1473-3099(20)30933-6).
- Deng, Y., Ran, W., Man, S., Li, X., Gao, H., Tang, W., Tachibana, H., Cheng, X., 2015. Artemether exhibits amoebicidal activity against acanthamoeba castellanii through inhibition of the serine biosynthesis pathway. *Antimicrob. Agents Chemother.* 59, 4680–4688. <https://doi.org/10.1128/AAC.04758-14>.
- Deschner, F., Risch, T., Baier, C., Schlüter, D., Herrmann, J., Müller, R., 2024. Nitroxoline resistance is associated with significant fitness loss and diminishes in vivo virulence of *Escherichia coli*. *Microbiol. Spectr.* 12, e0307923. <https://doi.org/10.1128/spectrum.03079-23>.
- Desideri, E., Filomeni, G., Ciriolo, M.R., 2012. Glutathione participates in the modulation of starvation-induced autophagy in carcinoma cells. *Autophagy* 8, 1769–1781. <https://doi.org/10.4161/auto.22037>.
- Elder, M.J., Kilvington, S., Dart, J.K., 1994. A clinicopathologic study of in vitro sensitivity testing and Acanthamoeba keratitis. *Invest. Ophthalmol. Vis. Sci.* 35, 1059–1064.
- Friesner, R.A., Murphy, R.B., Repasky, M.P., Frye, L.L., Greenwood, J.R., Halgren, T.A., Sanschagrin, P.C., Mainz, D.T., 2006. Extra precision glide: docking and scoring incorporating a model of hydrophobic enclosure for protein-ligand complexes. *J. Med. Chem.* 49, 6177–6196. <https://doi.org/10.1021/jm051256o>.
- Fuchs, F., Aldejohann, A.M., Hoffmann, A.M., Walthert, G., Kurzai, O., Hamprecht, A.G., 2022a. In vitro activity of nitroxoline in antifungal-resistant *Candida* species isolated from the urinary tract. *Antimicrob. Agents Chemother.* 66, e0226521. <https://doi.org/10.1128/aac.02265-21>.
- Fuchs, F., Becerra-Aparicio, F., Xanthopoulou, K., Seifert, H., Higgins, P.G., 2022b. In vitro activity of nitroxoline against carbapenem-resistant *Acinetobacter baumannii* isolated from the urinary tract. *J. Antimicrob. Chemother.* 77, 1912–1915. <https://doi.org/10.1093/jac/dkac123>.
- Fuchs, F., Hof, H., Hofmann, S., Kurzai, O., Meis, J.F., Hamprecht, A., 2021. Antifungal activity of nitroxoline against *Candida auris* isolates. *Clin. Microbiol. Infect.* 27, e10. <https://doi.org/10.1016/j.cmi.2021.06.035>, 1697.e7-1697.e10.
- Garcia, J.H., Akins, E.A., Jain, S., Wolf, K.J., Zhang, J., Choudhary, N., Lad, M., Shukla, P., Rios, J., Seo, K., Gill, S.A., Carson, W.H., Carrete, L.R., Zheng, A.C., Raleigh, D.R., Kumar, S., Agbi, M.K., 2023. Multi-omic screening of invasive GBM cells reveals targetable transsulfuration pathway alterations. *J. Clin. Invest.* e170397. <https://doi.org/10.1172/JCI170397>.
- Haston, J.C., Cope, J.R., 2023. Amebic encephalitis and meningoencephalitis: an update on epidemiology, diagnostic methods, and treatment. *CNS Infections* 36.
- He, P., Huang, S., Wang, R., Yang, Y., Yang, S., Wang, Y., Qi, M., Li, J., Liu, X., Zhang, X., Feng, M., 2024. Novel nitroxoline derivative combating resistant bacterial infections through outer membrane disruption and competitive NDM-1 inhibition. *Emerg. Microb. Infect.* 13, 2294854. <https://doi.org/10.1080/22221751.2023.2294854>.
- Hirukawa, Y., Nakato, H., Izumi, S., Tsuruhara, T., Tomino, S., 1998. Structure and expression of a cyst specific protein of *Acanthamoeba castellanii*. *Biochim. Biophys. Acta* 1398, 47–56. [https://doi.org/10.1016/s0167-4781\(98\)00026-8](https://doi.org/10.1016/s0167-4781(98)00026-8).
- Hoffmann, A.M., Wolke, M., Rybniker, J., Plum, G., Fuchs, F., 2023. Activity of the old antimicrobial nitroxoline against *Mycobacterium abscessus* complex isolates. *J. Glob. Antimicrob. Resist.* 33, 1–4. <https://doi.org/10.1016/j.jgar.2023.02.010>.
- Hu, Y., Wang, Lu, Han, X., Zhou, Y., Zhang, T., Wang, Li, Hong, T., Zhang, W., Guo, X.-X., Sun, J., Qi, Y., Yu, J., Liu, H., Wu, F., 2019. Discovery of a bioactive inhibitor with a new scaffold for cystathionine γ -lyase. *J. Med. Chem.* 62, 1677–1683. <https://doi.org/10.1021/acs.jmedchem.8b01720>.
- Huang, J.-M., Ko, P.-J., Huang, C.-L., Wen, P.-W., Chen, C.-H., Shih, M.-H., Lin, W.-C., Huang, F.-C., 2021. Cytochrome P450 monooxygenase of *Acanthamoeba castellanii* participates in resistance to polyhexamethylene biguanide treatment. *Parasite* 28, 77. <https://doi.org/10.1051/parasite/2021074>.
- Joaquim, A.R., Gionbelli, M.P., Gosmann, G., Fuentesria, A.M., Lopes, M.S., Fernandes de Andrade, S., 2021. Novel antimicrobial 8-hydroxyquinoline-based agents: current development, structure-activity relationships, and perspectives. *J. Med. Chem.* 64, 16349–16379. <https://doi.org/10.1021/acs.jmedchem.1c01318>.
- Johnson, A.A., Cuellar, T.L., 2023. Glycine and aging: evidence and mechanisms. *Ageing Res. Rev.* 87, 101922. <https://doi.org/10.1016/j.arr.2023.101922>.
- Kalra, S.K., Sharma, P., Shyam, K., Tejan, N., Ghoshal, U., 2020. Acanthamoeba and its pathogenic role in granulomatous amebic encephalitis. *Exp. Parasitol.* 208, 107788. <https://doi.org/10.1016/j.exppara.2019.107788>.
- Lampe, R.H., Coale, T.H., Forsch, K.O., Jabre, L.J., Kekuwa, S., Bertrand, E.M., Horák, A., Oborník, M., Rabines, A.J., Rowland, E., Zheng, H., Andersson, A.J., Barbeau, K.A., Allen, A.E., 2023. Short-term acidification promotes diverse iron acquisition and conservation mechanisms in upwelling-associated phytoplankton. *Nat. Commun.* 14, 7215. <https://doi.org/10.1038/s41467-023-42949-1>.
- Laurie, M.T., White, C.V., Retalack, H., Wu, W., Moser, M.S., Sakanari, J.A., Ang, K., Wilson, C., Arkin, M.R., DeRisi, J.L., 2018. Functional assessment of 2,177 U.S. And international drug identifies the quinoline nitroxoline as a potent amoebicidal agent against the pathogen *Balamuthia mandrillaris*. *mBio* 9, e02051. <https://doi.org/10.1128/mBio.02051-18>, 18.
- Laxman, S., Sutter, B.M., Wu, X., Kumar, S., Guo, X., Trudgian, D.C., Mirzaei, H., Tu, B.P., 2013. Sulfur amino acids regulate translational capacity and metabolic homeostasis through modulation of tRNA thiolation. *Cell* 154, 416–429. <https://doi.org/10.1016/j.cell.2013.06.043>.
- Leitsch, D., Mbouaka, A.L., Köhler, M., Müller, N., Walochnik, J., 2021. An unusual thioredoxin system in the facultative parasite *Acanthamoeba castellanii*. *Cell. Mol. Life Sci.* 78, 3673–3689. <https://doi.org/10.1007/s00018-021-03786-x>.
- Lim, N., Goh, D., Bunce, C., Xing, W., Fraenkel, G., Poole, T.R.G., Ficker, L., 2008. Comparison of polyhexamethylene biguanide and chlorhexidine as monotherapy agents in the treatment of *Acanthamoeba* keratitis. *Am. J. Ophthalmol.* 145, 130–135. <https://doi.org/10.1016/j.ajo.2007.08.040>.
- Liu, K., Abouelhassan, Y., Zhang, Y., Jin, S., Huigens Iii, R.W., 2022. Transcript profiling of nitroxoline-treated biofilms shows rapid up-regulation of iron acquisition gene clusters. *ACS Infect. Dis.* 8, 1594–1605. <https://doi.org/10.1021/acscinfed.2c00206>.
- Liu, Z., Tang, W., Liu, J., Han, Y., Yan, Q., Dong, Y., Liu, X., Yang, D., Ma, G., Cao, H., 2023. A novel sprayable thermosensitive hydrogel coupled with zinc modified metformin promotes the healing of skin wound. *Bioact. Mater.* 20, 610–626. <https://doi.org/10.1016/j.bioactmat.2022.06.008>.
- McCarthy-Leo, C., Darwiche, F., Tainsky, M.A., 2022. DNA repair mechanisms, protein interactions and therapeutic targeting of the MRN complex. *Cancers* 14, 5278. <https://doi.org/10.3390/cancers14215278>.
- Menolfi, D., Zha, S., 2020. ATM, ATR and DNA-PKcs kinases—the lessons from the mouse models: inhibition \neq deletion. *Cell Biosci.* 10, 8. <https://doi.org/10.1186/s13578-020-0376-x>.
- Needleman, S.B., Wunsch, C.D., 1970. A general method applicable to the search for similarities in the amino acid sequence of two proteins. *J. Mol. Biol.* 48, 443–453. [https://doi.org/10.1016/0022-2836\(70\)90057-4](https://doi.org/10.1016/0022-2836(70)90057-4).
- Niederhorn, J.Y., 2021. The biology of *Acanthamoeba* keratitis. *Exp. Eye Res.* 202, 108365. <https://doi.org/10.1016/j.exer.2020.108365>.
- O'Grady, F., Smith, B., 1966. Neuromyopathy in the mouse produced by the antimicrobial agent nitroxoline. *J. Pathol. Bacteriol.* 92, 43–48. <https://doi.org/10.1002/path.1700920106>.
- Ouyang, Y., Wu, Q., Li, J., Sun, Si, Sun, Shengrong, 2020. S-adenosylmethionine: a metabolite critical to the regulation of autophagy. *Cell Prolif.* 53, e12891. <https://doi.org/10.1111/cpr.12891>.
- Parkhitko, A.A., Jouandin, P., Mohr, S.E., Perrimon, N., 2019. Methionine metabolism and methyltransferases in the regulation of aging and lifespan extension across species. *Aging Cell* 18, e13034. <https://doi.org/10.1111/ace1.13034>.
- Paul, B.D., Sbodio, J.I., Snyder, S.H., 2018. Cysteine metabolism in neuronal redox homeostasis. *Trends Pharmacol. Sci.* 39, 513–524. <https://doi.org/10.1016/j.tips.2018.02.007>.
- Paulet, L., Trecoart, A., Leary, A., Peron, J., Descotes, F., Devouassoux-Shisheboran, M., Leroy, K., You, B., Lopez, J., 2022. Cracking the homologous recombination deficiency code: how to identify responders to PARP inhibitors. *Eur. J. Cancer* 166, 87–99. <https://doi.org/10.1016/j.ejca.2022.01.037>.
- Pelletier, C., Prognon, P., Bourlioux, P., 1995. Roles of divalent cations and pH in mechanism of action of nitroxoline against *Escherichia coli* strains. *Antimicrob. Agents Chemother.* 39, 707–713. <https://doi.org/10.1128/AAC.39.3.707>.

- Rodríguez-Expósito, R.L., Sifaoui, I., Reyes-Batlle, M., Fuchs, F., Scheid, P.L., Piñero, J.E., Satak, R., Lorenzo-Morales, J., 2023. Induction of programmed cell death in *Acanthamoeba culbertsoni* by the repurposed compound nitroxoline. *Antioxidants* 12, 2081. <https://doi.org/10.3390/antiox12122081>.
- Salazar, O.R., N Arun, P., Cui, G., Bay, L.K., van Oppen, M.J.H., Webster, N.S., Aranda, M., 2022. The coral *Acropora loripes* genome reveals an alternative pathway for cysteine biosynthesis in animals. *Sci. Adv.* 8, eabq0304. <https://doi.org/10.1126/sciadv.abq0304>.
- Siddiqui, R., Khan, N.A., 2012. Biology and pathogenesis of *Acanthamoeba*. *Parasites Vectors* 5, 6. <https://doi.org/10.1186/1756-3305-5-6>.
- Tain, L.S., Jain, C., Nespital, T., Froehlich, J., Hinze, Y., Grönke, S., Partridge, L., 2020. Longevity in response to lowered insulin signaling requires glycine N-methyltransferase-dependent spermidine production. *Aging Cell* 19, e13043. <https://doi.org/10.1111/acer.13043>.
- UniProt Consortium, 2023. UniProt: the universal protein knowledgebase in 2023. *Nucleic Acids Res.* 51, D523–D531. <https://doi.org/10.1093/nar/gkac1052>.
- Visvesvara, G.S., Moura, H., Schuster, F.L., 2007. Pathogenic and opportunistic free-living amoebae: *Acanthamoeba* spp., *Balamuthia mandrillaris*, *Naegleria fowleri*, and *Sappinia diploidea*. *FEMS Immunol. Med. Microbiol.* 50, 1–26. <https://doi.org/10.1111/j.1574-695X.2007.00232.x>.
- Wang, M., Liang, X., Cheng, M., Yang, L., Liu, H., Wang, X., Sai, N., Zhang, X., 2019. Homocysteine enhances neural stem cell autophagy in in vivo and in vitro model of ischemic stroke. *Cell Death Dis.* 10, 561. <https://doi.org/10.1038/s41419-019-1798-4>.
- Wang, Y.-J., Chen, C.-H., Chen, J.-W., Lin, W.-C., 2021. Commensals serve as natural barriers to mammalian cells during *Acanthamoeba castellanii* invasion. *Microbiol. Spectr.* 9, e0051221. <https://doi.org/10.1128/Spectrum.00512-21>.
- Wolff, N.A., Ghio, A.J., Garrick, L.M., Garrick, M.D., Zhao, L., Fenton, R.A., Thévenod, F., 2014. Evidence for mitochondrial localization of divalent metal transporter 1 (DMT1). *Faseb. J.* 28, 2134–2145. <https://doi.org/10.1096/fj.13-240564>.
- Zhang, H., Cheng, X., 2021. Various brain-eating amoebae: the protozoa, the pathogenesis, and the disease. *Front. Med.* 15, 842–866. <https://doi.org/10.1007/s11684-021-0865-2>.
- Zhang, X., Zhao, Q., Wang, T., Long, Q., Sun, Y., Jiao, L., Gullerova, M., 2023. DNA damage response, a double-edged sword for vascular aging. *Ageing Res. Rev.* 92, 102137. <https://doi.org/10.1016/j.arr.2023.102137>.
- Zhang, Y., Xu, X., Wei, Z., Cao, K., Zhang, Z., Liang, Q., 2023. The global epidemiology and clinical diagnosis of *Acanthamoeba keratitis*. *J Infect Public Health* 16, 841–852. <https://doi.org/10.1016/j.jiph.2023.03.020>.
- Zhu, J., Berisa, M., Schwörer, S., Qin, W., Cross, J.R., Thompson, C.B., 2019. Transsulfuration activity can support cell growth upon extracellular cysteine limitation. *Cell Metabol.* 30, 865–876.e5. <https://doi.org/10.1016/j.cmet.2019.09.009>.